CHEMISTRY OF MATERIALS
Cite This: Chem. Mater. 2019, 31, 8937−8947
Article
pubs.acs.org/cm

Elucidating the Evolving Atomic Structure in Atomic Layer Deposition Reactions with in Situ XANES and Machine Learning

Orlando Trejo,[¶,†] Anup L. Dadlani,[¶,‡] Francisco De La Paz,[§] Shinjita Acharya,[§] Rob Kravec,[∥] Dennis Nordlund,[⊥] Ritimukta Sarangi,[⊥] Fritz B. Prinz,[§,#] Jan Torgersen,[‡] and Neil P. Dasgupta*[,†]

[†]Department of Mechanical Engineering, University of Michigan, Ann Arbor, Michigan 48109, United States
[‡]Department of Mechanical and Industrial Engineering, NTNU, Trondheim 7491, Norway
[§]Department of Mechanical Engineering, Stanford University, Stanford, California 94305, United States
[∥]Department of Chemical Engineering, Stanford University, Stanford, California 94305, United States
[⊥]Stanford Synchrotron Radiation Lightsource, SLAC National Accelerator Laboratory, Menlo Park, California 94025, United States
[#]Department of Materials Science and Engineering, Stanford University, Stanford, California 94305, United States

Supporting Information

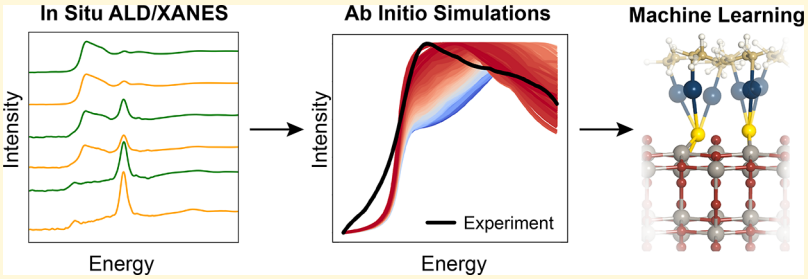

ABSTRACT: Precision synthesis of thin films requires an improved mechanistic understanding of the structural evolution of materials at the atomic scale. Atomic layer deposition (ALD) is a critical nanofabrication technique that enables fine-tuning of atomic structure and thickness as a result of its layer-by-layer growth behavior. In this study, in situ X-ray absorption spectra of the S K-edge during ALD growth of ZnS thin films on TiO_2 nanoparticles were collected and analyzed. The experimental results show that both sulfide and sulfate species form during the nucleation phase of ZnS on TiO_2. As film growth proceeds, the S K-edge of the in situ ZnS film converges to that of a representative ex situ ALD ZnS film. By building representative atomistic models, a high-throughput screening method was developed to determine the most probable atomic configurations as the film structure evolves. The screening method consisted of a supervised machine learning analysis of thousands of simulated X-ray absorption near edge structure (XANES) spectra. Atomic-level insight was gained into changes in the coordination environment of surface species as they transitioned from the nucleation phase toward the crystalline ZnS phase. The experimental and computational strategies presented herein provide an example of how in situ synchrotron-based characterization can be leveraged using robust modeling approaches to elucidate the ordering of atoms during thin-film growth.

INTRODUCTION

Ultrathin films (<10 nm) play a critical role in a range of applications, including thin film solar cells,[1,2] wearable transistors,[3] and quantum computers.[4] Scaling and commercializing these next-generation technologies requires the ability to reliably control the atomic structure of thin film surfaces and interfaces over large areas. Atomic layer deposition (ALD) is a technique that overcomes critical challenges in thin film growth associated with the difficulties of simultaneously controlling thickness, composition, and conformality.[5] A crucial step toward achieving ultrafine control over matter at the atomic level using ALD is to understand the evolution of atomic coordination during film growth. However, while atomistic modeling and vibrational spectroscopy have provided valuable insights into the initial ALD surface reactions,[6,7] there is a lack of experimental techniques that can directly probe the dynamic rearrangement of the atomic structure during film growth, as atoms move from their initial reaction sites into crystalline lattice positions (Scheme 1).

X-ray absorption near-edge structure (XANES) is an enabling, element-specific spectroscopy technique for acquiring local bonding information. We have previously shown that ex situ S K-edge characterization of sulfides grown by ALD can capture subtle changes in local atomic and electronic structures during growth.[8−10] This precise analytical resolution is possible because S K-edge XANES spectra are highly sensitive to changes in the local coordination environment and oxidation state.[11] Furthermore, information on the local coordination

Received: July 29, 2019
Revised: October 14, 2019
Published: November 4, 2019

DOI: 10.1021/acs.chemmater.9b03025
Chem. Mater. 2019, 31, 8937−8947

Scheme 1. Representative Schematic of H_2S and Diethylzinc (DEZ) Half Cycle Reactions on an Anatase (101) TiO_2 Surface[a]

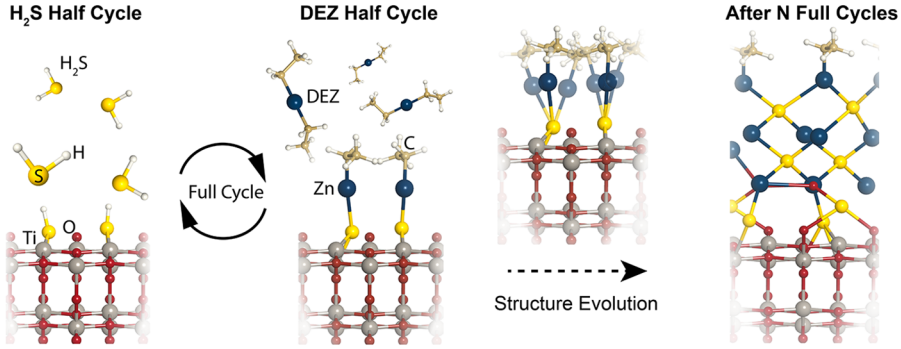

[a]In the initial half-cycles, atomic arrangements are driven by ligand-exchange reactions with surface functional groups. After N full cycles of H_2S and DEZ, a structure that converges to crystalline ZnS will form. This study presents a new approach to capture and analyze the structural evolution that occurs as film growth progresses.

environment in XANES spectra can be extracted using advances in theoretical modeling of X-ray absorption.[12−15] Because of this, in situ XANES of metal sulfides is an ideal methodology to improve our detailed understanding of the nucleation and growth behavior of thin films.

Previous work on in situ characterization of ALD materials has also provided valuable insight into the microstructure and morphology that evolves during ALD nucleation and growth.[16−18] For example, Boichot et al. used a combination of in situ X-ray techniques on ALD ZnO.[18] The study captured the process in which the overall ZnO grain structure is affected by interfacial strains due to the structure and chemistry of the substrate surfaces. In another study, Mack et al. investigated the grain structure evolution during in situ ALD film growth using STM on ALD ZnS, which elucidated the densely packed ZnS structure on gold surfaces at the nanoscale.[19] Given these advances of in situ characterization of grain structure, a natural next step is to understand how surface species self-organize as crystalline grains form. Toward this goal, in this study, we perform in situ characterization of ZnS growth in a customized ALD reactor together with S K-edge XANES to gain a detailed understanding of the structural evolution of the S species during nucleation and film growth.

The extraction of structural information from the rich XANES spectra is difficult and has hampered the intimate understanding of structure growth at the nanoscale.[20] The surface structure is inherently local and often consists of random and disordered atomic arrangements. To address the challenge of exploring a myriad of configurations, researchers have combined big-data analytic strategies with first-principles simulation packages (such as FEFF9) in order to provide statistical insights into the most likely and prominent atomic structures of bulk materials.[21−23] These high-throughput screenings of atomic configurations present a viable strategy to deepen our understanding of the possible atomic arrangements that may occur during film growth, which evolve during the dynamic surface reactions and nucleation of surface species.

Herein, we have measured and modeled the S K-edge XANES data during the nucleation phase of ZnS deposition on TiO_2 nanoparticle (NP) surfaces. The choice of ZnS and TiO_2 as a model system is due to the technological relevance of this material combination in thin-film solar cells.[24−26] Improved understanding of the interfacial structural evolution of this material system can facilitate the rational design of photovoltaic cells. Furthermore, we can leverage the self-limiting, linear growth, and volatile precursor chemistry of ALD ZnS when designing the measurement and modeling experiments.[27,28] Lastly, the high surface area of the TiO_2 NPs increases the signal-to-noise ratio, which improves our ability to capture subtle cycle-by-cycle changes in the XANES spectra.

To approximate the evolving atomic surface structure during the initial cycles, we developed a high-throughput screening method that incorporated the design of experiments (DoEs) for sensitivity screening, neural networks, and random forests to determine likely atomic structures and their corresponding geometric parameters (e.g., bond lengths and bond angles). This approach captures the transition from a sulfate-rich nucleation phase on the TiO_2 anatase surface to the sulfide-dominant ZnS film. This work provides an example of how in situ XANES measurements and machine learning (ML) can be leveraged synergistically to yield atomistic insight into surface reactions and structural evolution during thin-film growth.

METHODS

In Situ XANES Measurements. A modular ALD system was constructed that can safely be used to deposit and characterize ALD of sulfide materials at multiple beamlines at the Stanford Synchrotron Radiation Lightsource (SSRL). Owing to the safety concerns surrounding the use of H_2S, extra considerations were taken for the materials and components used in the ALD system design.[29] Figure 1 shows a photograph and schematic of the ALD system used for this work. The hot-walled reactor consisted of a heated sample holder. A heated manifold delivered precursors to the chamber, and a pressure gauge monitored the reaction chamber pressure. The two precursors used were H_2S, which was generated in situ in the precursor source cylinder via the thermal decomposition of thioacetamide (Sigma-Aldrich, U.S.A.),[27,28] and diethylzinc (DEZ) (Sigma-Aldrich, U.S.A.). The pulsing conditions consisted of 0.25-s H_2S pulses, 0.1-s DEZ pulses, and 60-s He purges. A total fluorescence yield (TFY) detector captured the S K-edge XANES spectra. Standard postprocessing of the XANES spectra was done using the SixPACK and Athena analysis packages. Additional details on the experimental setup are in the Supporting Information (SI).

FEFF Simulations and Machine Learning. Theoretical XANES spectra were generated using the FEFF9 code based on Green's function multiple-scattering theory.[13,14] To calibrate the parameters for the FEFF9 models, the S K-edge simulated spectra for ZnS was converged by varying the cluster, self-consistent field (SCF), and scattering sphere sizes and obtaining spectral agreement between the simulated and experimental sphalerite ZnS. A custom platform was developed to enable high-throughput generation, modeling, and

DOI: 10.1021/acs.chemmater.9b03025
Chem. Mater. 2019, 31, 8937−8947

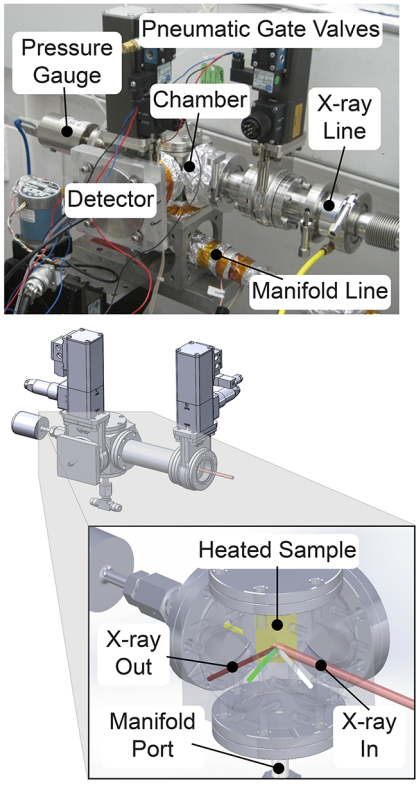

Figure 1. Photograph and schematic representation of the modular and sulfide-compatible ALD system built for in situ synchrotron radiation studies. Critical components of the design: the pneumatic gate valves that enable automated X-ray absorbance and detection; the heated sample holder; and the heated chamber and manifold line.

analysis of atomic configurations. The goal of this platform is to enable a seamless integration of the ability to customize atomic structures with machine learning and ab initio simulations using FEFF9. This code was built using open-source packages for creating CIF and FEFF input files (Pymatgen[30]), design of experiments (pyDOE), and machine learning (ML) models (scikit-learn[31]). The atomic structures were illustrated using VESTA.[32] Further details on the platform are in the SI. To confirm the validity of this custom framework, we compared the results from our platform to the results obtained from the commercially available JMP[33] software package as described below.

Following ML best practice guidelines for chemical and materials science research,[34] we created a workflow to tune and analyze the structural parameters of representative S moieties during ALD growth (Scheme 2 and Scheme SI1). We used two robust and straightforward regression ML models: random forests (RFs) and artificial neural networks (NNs). Random forests consist of many decision trees that learn rules from input features to predict the values of a target input; they also provide information about the relative importance of each feature.[35] However, the use of parameter importance information in RF models needs to be done with caution when working with nonlinear systems.[36] In this work, we use parameter importances determined by the RF models solely to aid the discussion of the simulation results, and to provide physical insight. The parameter importances do not play an active role in our modeling process. We have validated the use of parameter importances for our particular systems through a full factorial analysis comparison (further details in Supporting Information).

In our case, the input features are adjustments to the geometric parameters of the S moieties. The target value is the coefficient of determination (R^2) between the simulated and corresponding experimental S K-edge spectra. In other words, given a guess of the structure of the S moieties, we calculate the R^2 value of how well the simulated S K-edge spectrum matches the experimental curve over a defined energy range. From now on this R^2 value will be referred to as the "Fit" of the simulated curves. Further ML model setup and result details are in the SI, including corresponding mean square error (MSE) and root-mean-square error (RMSE) values and plots.

We used RF and NN models on six data sets that contained 1100 different atomic arrangements on average. The data sets were built and analyzed for the first half cycle (H_2S_1), the second half cycle of DEZ (DEZ_2), the fourth half cycle (DEZ_4), and the sixth half cycle (DEZ_6). Model parameters were tuned using the training and

Scheme 2. Overview of the Workflow[a]

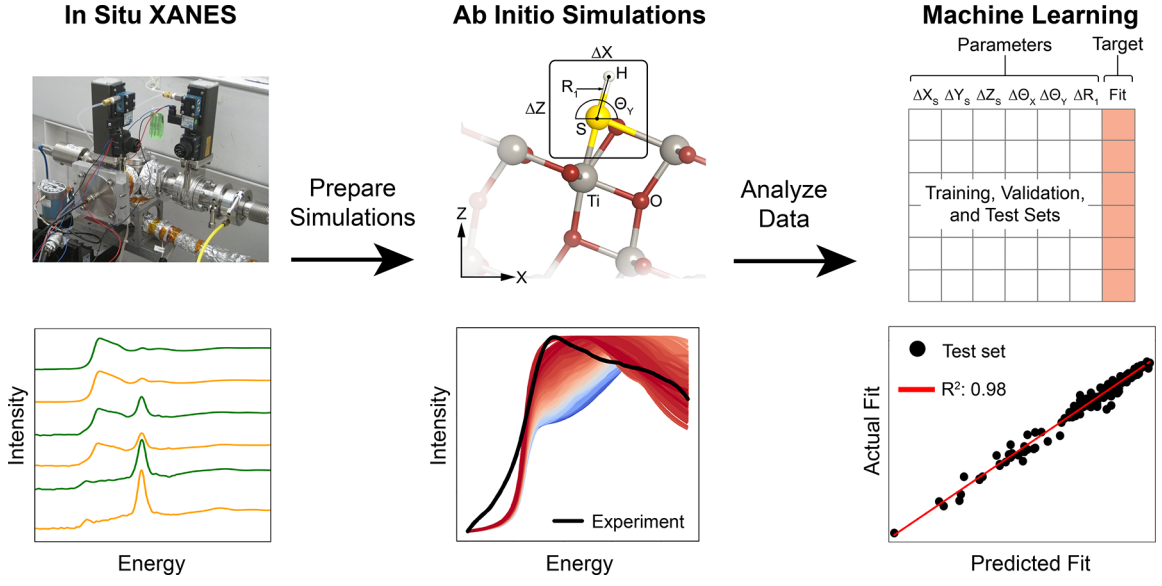

[a]Simulations are prepared by using information from in situ XANES spectra and creating FEFF input files with Pymatgen and pyDOE. After running the simulations, the next step in the framework is to analyze all the data using random forests or neural networks with scikit-learn and JMP, respectively. This allows one to explore a substantially larger parameter space and hence get a comprehensive understanding of the system. A more detailed description of the modeling and machine learning workflow is depicted in the Supporting Information.

DOI: 10.1021/acs.chemmater.9b03025
Chem. Mater. 2019, 31, 8937−8947

validation sets only. The test set was used to verify how well the ML models generalize to unseen data. Table SI2 (Supporting Information) summarizes how well the RF and NN ML models can capture the impact of changes to the structural parameters on the Fit of the simulated spectra. The tabulated performance metrics are the R^2 values between the actual Fit values and the predicted Fit values by the ML models. Essentially, we create an ML model of FEFF9 models in order to explore a larger atomic configuration space more efficiently. This more efficient exploration cuts down the computational time required to run a FEFF9 simulation every time.[37] As Table SI2 shows, the RF and NN perform similarly, so we have confidence that the RF model parameters have been appropriately tuned and generalize well to unseen data. Further details, including the actual vs predicted plots of the ML models, plots of the RFs complexity curves, perceptron schematics of the NN models, and model validation are provided in the Supporting Information.

RESULTS

XANES Spectra. Figure 2 shows the experimentally measured in situ S K-edge TFY spectra for the initial half cycle and full cycles of ZnS growth, as well as two ex situ ALD ZnS references. As depicted in Scheme 1, a half cycle is an exposure of either H_2S or DEZ to the surface followed by inert gas purging. During the initial cycles, the XANES spectra show that the film nucleates with a mix of sulfide and sulfate species. XPS analysis confirms the existence of sulfate species in the initial cycles of ex situ ALD ZnS from a reference reactor, as shown in Figure SI5. Therefore, the sulfate species observed in Figure 2 are not likely a result of trace water or a leak in the in situ ALD system. It is also important to note that the sulfate intensity in S K-edge spectra is several times higher than the sulfide intensity due to the stronger transition dipole arising from polar bonding.[11] As can be seen in the first half cycles (H_2S_1), titanium sulfide (TiS_x) with an expected absorption onset edge around 2470 eV[38] and titanium sulfate $Ti(SO_4)_x$ with an expected onset absorption edge around 2481 eV[39] are formed. It is possible that the feature labeled as TiS_x feature is also due to physiosorbed H_2S on TiO_2.

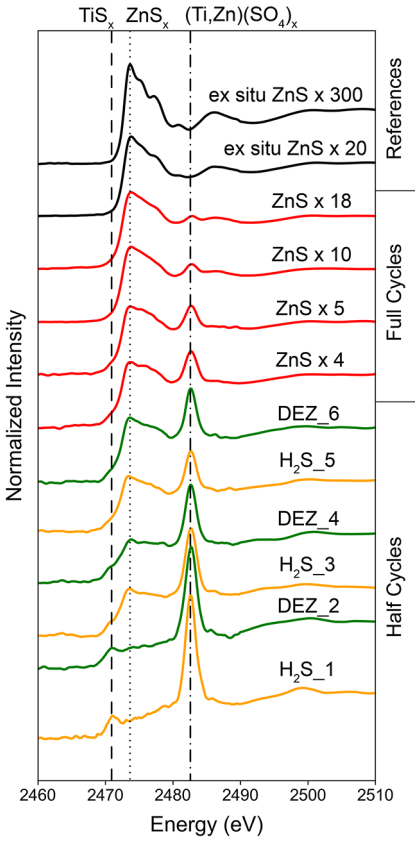

Figure 2. S K-edge spectra of ZnS half cycles, full cycles, and ex situ references. The titanium and zinc sulfide regions are traced by dashed and dotted lines, respectively. The dashed-dotted line labels the sulfate region. The experimental in situ spectra capture how the initial sulfide and sulfate regions evolve and converge toward ZnS.

The TiS_x and $Ti(SO_4)_x$ regions of the S K-edge spectra are delineated with dashed and dashed-dotted lines, respectively. The overall shape of S K-edge curve remains the same after pulsing DEZ in the second ALD half cycle (DEZ_2). This shape similarity suggests either that the DEZ is not reacting with the surface or that DEZ exposure does not change the coordination environment of the TiS_x and $Ti(SO_4)_x$ significantly. As can be seen after exposing the surface to H_2S again in the third half cycle (H_2S_3), a distinct ZnS_x feature is observed with an expected absorption onset around 2473 eV, which is consistent with the reference ZnS samples at the top of Figure 2.

In the H_2S_3 half cycle, there is evidence for three distinct sulfur phases: TiS_x, ZnS_x, and (Ti, Zn)$(SO_4)_x$. The presence of the ZnS_x peak disproves the hypothesis that DEZ did not react in the DEZ_2 half cycle. Therefore, DEZ reacted in the second half cycle to form surface monoethylzinc (II-MEZ) species. This pattern can be observed again after pulsing DEZ in the fourth (DEZ_4) and sixth (DEZ_6) half cycles. No significant changes to the S K-edge spectra from the preceding half cycles occurred, other than a slight decrease in the sulfate intensity, which is the result of a growing ZnS film on top of the buried sulfate interface (further analysis is in Figure SI4 and Table SI1). Only after the H_2S pulse in each full cycle can we confirm with greater certainty that DEZ reacted on the surface. This qualitative analysis guides the atomic modeling and analysis below using first-principles XANES simulations and ML, which provide a more quantitative framework for interpretation.

Figure 2 also shows the S K-edge spectra after 4, 5, 10, and 18 full cycles. The sulfate feature decreases as the ZnS feature becomes more pronounced. By 18 full cycles (ZnS × 18), the in situ S K-edge spectrum closely resembles that of a reference sample that was deposited ex situ with 20 cycles of ZnS (ZnS×x 20). For a quantitative comparison, we calculated and plotted the Pearson coefficient between the in situ spectra and the ex situ ZnS × 20 spectrum (Figure SI6). However, some slight differences exist when comparing the in situ ZnS × 18 to the ex situ ZnS × 20 S K-edge spectra. The origin of these differences is likely due to the pressurization of the reaction chamber at each measurement; the pressurization allows the opening of the gate valves to the beamline and detector. The change in pressure and exposure to the X-ray beam could have resulted in restructuring or desorption of reactive surface species (further details in Figure SI3). While there is a possibility of residual water or a small leak in the system, especially during the pressurization cycles, the data presented in Figures SI3, SI5, and SI6 (Supporting Information) suggest that the chemistry taking place during the in situ experiments is a valid approximation to the chemistry that takes place in a more ideal ALD reactor. Thus, in future in situ chamber designs, we aim to collect the spectra without having to repressurize the reaction chamber. It is also important to note that XANES can capture subtle changes in growth behavior

DOI: 10.1021/acs.chemmater.9b03025
Chem. Mater. 2019, 31, 8937−8947

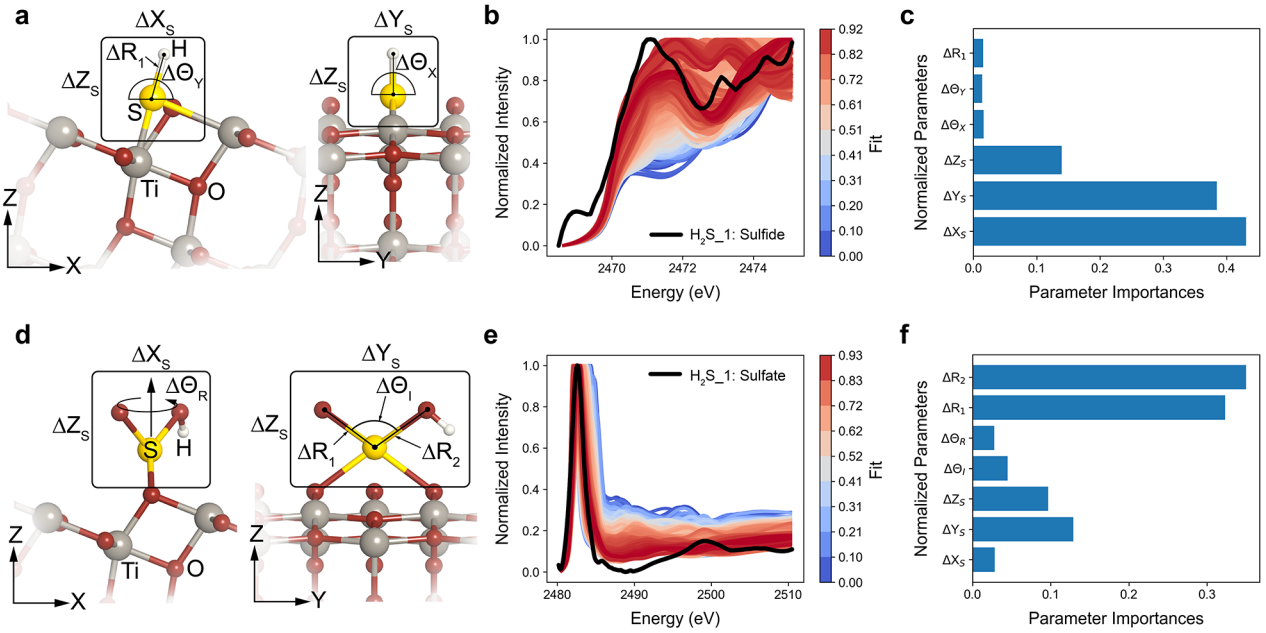

Figure 3. Sulfide (a–c) and sulfate (d–f) models in the H_2S_1 half-cycle. (a, d) Atomic schematics of the structural parameters modeled. (b, e) S K-edge spectra of the sulfide and sulfate experimental regions compared to simulations with the R^2 fit distribution. (c, f) The relative importance of the normalized structural parameters using Random Forests. For all plots that compare the simulated to the experimental spectra, the Fit values of the individual spectra are color-coded from blue ($R^2 = 0$) to red (maximum R^2). The energy range for the sulfide region is limited to below 2476 eV in order to minimize the influence of the sulfate pre-edge features and background on the fitting calculations.[39]

due to changes in processing conditions; such sensitivity can be exploited in the future to identify process conditions that facilitate the fabrication of higher quality interfaces or patterning of thin films in general.

The subsequent sections cover a detailed analysis of the selected half cycles. Using the machine learning framework, we show how modeling of the XANES spectra can be used to provide insight into the structural evolution of the film as it grows.

H_2S_1. As can be seen in Figure 2, sulfide and sulfate species form after the first half cycle of H_2S (H_2S_1). Based on experimental and computational studies of H_2S reactions on metal oxide surfaces,[40−44] we propose the following representative reactions to help explain the formation of the sulfide and sulfate species, where ‖ represents the substrate surface:

$$\|\text{-}TiO_2 + 2H_2S \rightarrow \|\text{-}TiS_2 + 2H_2O \quad \text{(sulfide formation)} \tag{1}$$

$$2H_2S + \|\text{-}TiO_2 + 6H_2O \rightarrow \|\text{-}Ti(SO_4)_2 + 8H_2 \quad \text{(sulfate formation)} \tag{2}$$

The atomic structures used for the FEFF9 simulations account for the hydrogenated surface species that participate in the ALD reactions. As shown in Figure 3a, we modeled the sulfide species as a bridged sulfhydryl (−SH) group bonded to Ti atoms on the surface, which is one of many possible initial configurations. Similarly, the sulfate species is modeled as a bridged S atom on two surface O atoms and capped by two ligand O atoms that formed after reacting with H_2O molecules according to eq 2 (Figure 3d). The models assume a surface along the TiO_2 anatase (101) plane, which is expected to be a prevalent surface for TiO_2 NPs.[45]

For the H_2S_1 sulfide model in Figure 3a, the structural parameters that are adjusted and fed into the RF and NN models consist of changes to the *XYZ* coordinates of the S atom (ΔX_S, ΔY_S, and ΔZ_S), the S−H bond length (ΔR_1), and the angle of the H atoms ($\Delta\Theta_X$ and $\Delta\Theta_Y$) with respect to the *X* and *Y* axes shown. The changes to these structural parameters were fed into the ML models to determine which geometric configurations resulted in the best fits between the simulated spectra and the corresponding experimental spectrum. For the sulfide region of H_2S_1, we overlay the experimental spectrum in black over the simulated S K-edge spectra in Figure 3b. For all plots that compare the simulated to the experimental spectra, the Fit values of the individual spectra are color-coded from blue ($R^2 = 0$) to red (maximum R^2). Larger Fit values correspond to a better match between the general shape of the experimental and simulated spectra. We do not expect perfect fits given the limitations of the FEFF9 theory and the complexity of the actual surface atomic structure. Figure 3c shows the parameter importances in our RF model, which is a measure of how sensitive the Fit is to the geometric parameters. According to the trained RF model, the most important structural parameters were changes to the *XYZ* coordinates of the S atoms. The Fit values were not sensitive to changes to the H bond length or axial bond angles. This ability to identify viable atomic structures based on subtle changes illustrates the power of the ML framework to rapidly screen geometric configurations and provide valuable mechanistic insight into the structural evolution of the ALD film.

The structural parameters that were adjusted in the sulfate model in Figure 3d consist of changes to the *XYZ* coordinates of the S atom, the internal O−S−O angle ($\Delta\Theta_I$) with respect to the ligand O atoms, the rotational angle ($\Delta\Theta_R$) of the ligand O atoms about the S *Z*-axis, and the S−O bond lengths (ΔR_1 and ΔR_2) of the ligand O atoms. Figure 3e shows the overlaid simulated and experimental spectra. According to the H_2S_1

DOI: 10.1021/acs.chemmater.9b03025
Chem. Mater. 2019, 31, 8937−8947

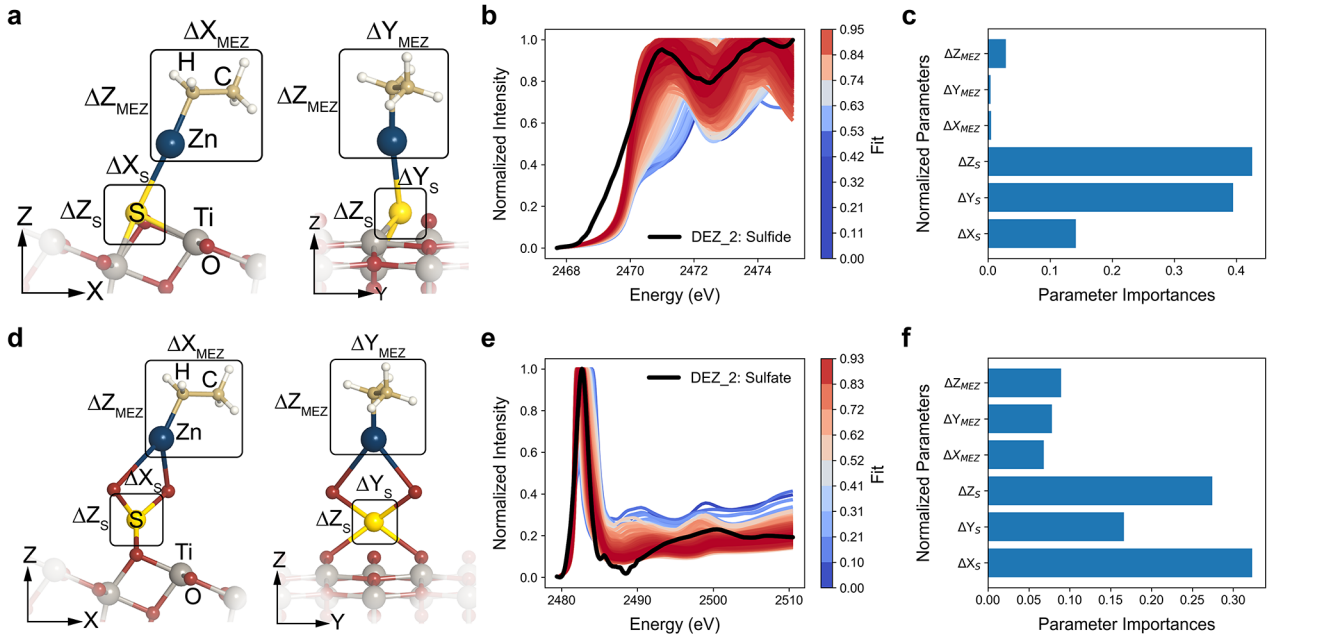

Figure 4. Sulfide (a–c) and sulfate (d–f) models in the DEZ_2 half-cycle. (a, d) Atomic schematics of the structural parameters modeled. (b, e) S K-edge spectra of the sulfide and sulfate experimental regions compared to simulations with the R^2 fit distribution. (c, f) The relative importance of the normalized structural parameters using Random Forests. For all plots that compare the simulated to the experimental spectra, the Fit values of the individual spectra are color-coded from blue ($R^2 = 0$) to red (maximum R^2). The energy range for the sulfide region is limited to below 2476 eV in order to minimize the influence of the sulfate pre-edge features and background on the fitting calculations.[39]

sulfate model parameter importances (Figure 3f), the bond lengths between the S atom and the ligand O atoms (ΔR_1 and ΔR_2) are the most important structural parameters with combined importance greater than 60%. There is a significant influence from changes to the *Y* and *Z* positions of the S atom, but they are each less than half of the relative importance of either ΔR_1 or ΔR_2. Adjustments to ΔX_S, $\Delta\Theta_I$, and $\Delta\Theta_R$ all have less than 5% importance when determining the Fit score of the simulated S K-edge spectra.

In the subsequent analysis, the best fits from the previous half cycle initiate the atomic configurations, which were then adjusted based on representative reactions for each half cycle. We confirmed the validity of the initial atomic models by manually inspecting the bond lengths and angles and ensuring that they are within reasonable ranges as determined by experiments and previous DFT studies.[17,18,46] While the DFT simulations are limited in capturing a large number of distinct atomic configurations, their use as starting points for XANES simulations is verified by the similarity between the experimental and simulated spectra in Figures 3–6. The inspection of configurations will be automated in the future to facilitate the screening of more configurations, but it needs to be done carefully in order to avoid false positives.

DEZ_2. In the second half cycle (DEZ_2), the substrate was exposed to DEZ for the first time. The following representative reactions are used to describe the overall chemical reactions:

$$\|\text{-Ti-SH} + \text{Zn}(\text{C}_2\text{H}_5)_2 \rightarrow \|\text{-TiS-Zn-C}_2\text{H}_5 + \text{CH}_4(\text{g}) \quad (3)$$

$$\|\text{-Ti}(\text{SO}_3)\text{-OH} + \text{Zn}(\text{C}_2\text{H}_5)_2 \rightarrow \|\text{-TiSO}_4\text{-Zn-C}_2\text{H}_5 + \text{CH}_4(\text{g}) \quad (4)$$

For the DEZ_2 sulfide model described by eq 3, a monoethylzinc (MEZ) group replaced the H atom (Figure 4a). Similarly, in the DEZ_2 sulfate model described by eq 4, a MEZ ligand replaced the H atom in one of the O ligands, and the MEZ ligand sits in a bridge position between both O ligand atoms (Figure 4d). This structure was adapted from a possible O–Zn–O configuration calculated by first-principles studies of the ALD ZnO process.[46]

For this round of modeling, the changes to the *XYZ* coordinates of the S (ΔX_S, ΔY_S, and ΔZ_S) and MEZ (ΔX_{MEZ}, ΔY_{MEZ}, and ΔZ_{MEZ}) species were the structural parameters that were varied, keeping all other atomic positions fixed during the simulations. In reality, we expect that all of the coordinating atoms will find new positions relative to the surface atoms, in order to accommodate the influence of the MEZ species. However, as shown in Figure 4b, limiting the parameter space in this manner was sufficient to provide a Fit value of 0.95 when comparing the simulated and experimental XANES spectra. This straightforward screening demonstrates the power of our framework to sort and identify likely atomic arrangements that are descriptive of the evolving atomic structure. In the future, these configurations will provide a valuable starting point as an input to DFT studies of fully relaxed structures.

As shown in Figure 4c, changes to the *XYZ* coordinates of the S atom are more important than changes to the MEZ coordinates. Rotational variations of the MEZ were also explored but had negligible importance values on the Fit. In DEZ_2, changes in Y_S and Z_S were about four times more important than changes in X_S. In contrast, in the H_2S_1 half cycle, changes in X_S and Y_S were at least three times more important than changes in Z_S. In the Discussion section, surface response plots will be presented to provide further detail on how changes in the S atom positions affect the Fit

DOI: 10.1021/acs.chemmater.9b03025
Chem. Mater. 2019, 31, 8937–8947

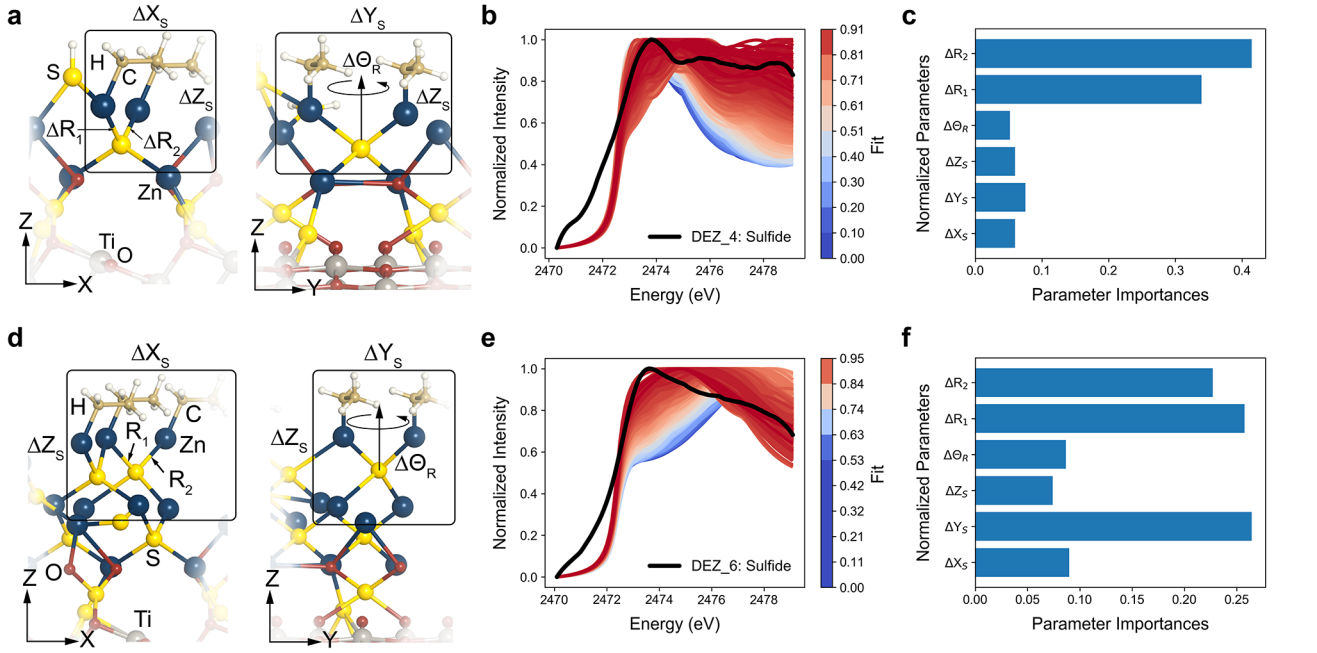

Figure 5. DEZ_4 (a–c) and DEZ_6 sulfide models (d–f). (a, d) Atomic schematics of the structural parameters modeled. (b, e) S K-edge spectra of the sulfide experimental regions compared to simulations with the R^2 fit distribution. (c, f) The relative importance of the normalized structural parameters using Random Forests. For all plots that compare the simulated to the experimental spectra, the Fit values of the individual spectra are color-coded from blue (R^2 = 0) to red (maximum R^2).

values. Both the H_2S_1 and DEZ_2 model results suggest that the structural changes that have the most significant influence on the XANES spectra are the S–Ti bond lengths.

There are also slight changes in the S K-edge spectra within the sulfate regions of H_2S_1 (Figure 3e) and DEZ_2 (Figure 4e). According to the DEZ_2 models, the importance of the MEZ species is more significant in the sulfate model than in the sulfide model. However, the most important structural parameters are still adjustments to the *XYZ* coordinates of the S atom. The combined importance for ΔX_S, ΔY_S, and ΔZ_S is higher than 70%.

DEZ_2 is the last round of simulations in which we model sulfate species since the relative intensity of the sulfate region in the XANES spectra decreases with subsequent cycles. Furthermore, since the experimental spectrum after each DEZ pulse resembles the spectrum from the previous H_2S half cycle, we will focus on the DEZ_4 and DEZ_6 half cycles in the subsequent simulations and ML modeling.

DEZ_4 and DEZ_6. The second DEZ pulse (DEZ_4) completed two full cycles; the third DEZ pulse (DEZ_6) completed three full cycles. The chemical reaction on the surface during DEZ_4 and DEZ_6 can be represented as follows:

$$\|\text{-SH} + x\text{Zn}(\text{C}_2\text{H}_5)_2 \rightarrow \|\text{-S-(Zn-C}_2\text{H}_5)_x + x\text{CH}_4(\text{g}) \quad (5)$$

Weckman et al. used DFT modeling to show that multiple MEZ species can coordinate on surface O atoms during ZnO growth.[46] We expect a similar mechanism to occur between MEZ species and surface S atoms during ZnS growth. The expected coordination of multiple MEZ species on the surface is why eq 5 does not specify the stoichiometry. In the actual atomic models, we assume that two DEZ molecules have reacted on the S atom of interest. When manually building the atomic models using atomic arrangements from the previous simulations, we assume that the surface species self-organize such that S is 4-fold coordinated. The assumption of 4-fold self-organization is consistent with in situ X-ray diffraction (XRD) and scanning tunneling microscopy (STM) measurements of the nucleation phase during ALD of ZnO[18] and ZnS.[28] While the initial input configurations to our model were manually determined based on reported data and knowledge of the final phase that eventually forms, future work is needed to automate the screening and implementation of different self-organizing heuristics in order to identify and explore a broader range of viable atomic arrangements.

As shown in Figure 5a, for DEZ_4, we have modeled a sulfur atom that is coordinated by two surface Zn atoms and two MEZ groups. In this atomic model, the structural parameters that were varied were (1) the changes to the *XYZ* coordinates of the S atom (ΔX_S, ΔY_S, and ΔZ_S); (2) the S–Zn bond lengths between the S and MEZ groups (ΔR_1 and ΔR_2); and (3) the rotational angle of the upper MEZ atoms about the S *Z*-axis ($\Delta\Theta_R$).

As shown in Figure 5b, the structure of the S–K edge in DEZ_4 flattens in the range between 2475 to 2480 eV. By close examination of the plot in Figure 5b, it is clear that multiple atomic structures produce simulated spectra capable of capturing the plateau of the S K-edge in this range. The flattening of the S–K edge is qualitative evidence of a turning point in the structural evolution of the ZnS film by the DEZ_4 half cycle. In DEZ_2, there is a slight oscillatory profile past the edge. In contrast, there is a clear downward profile in DEZ_6 (Figure 5e). Figure 5c indicates that the most important parameters that influence the Fit for DEZ_4 are the bond lengths between the Zn atoms of the MEZ groups and the 4-fold coordinated S atoms (ΔR_1 and ΔR_2). The total of the parameter importances of ΔR_1 and ΔR_2 is above 70%. The individual importances of the remaining structural parameters are below 10%.

DOI: 10.1021/acs.chemmater.9b03025
Chem. Mater. 2019, 31, 8937–8947

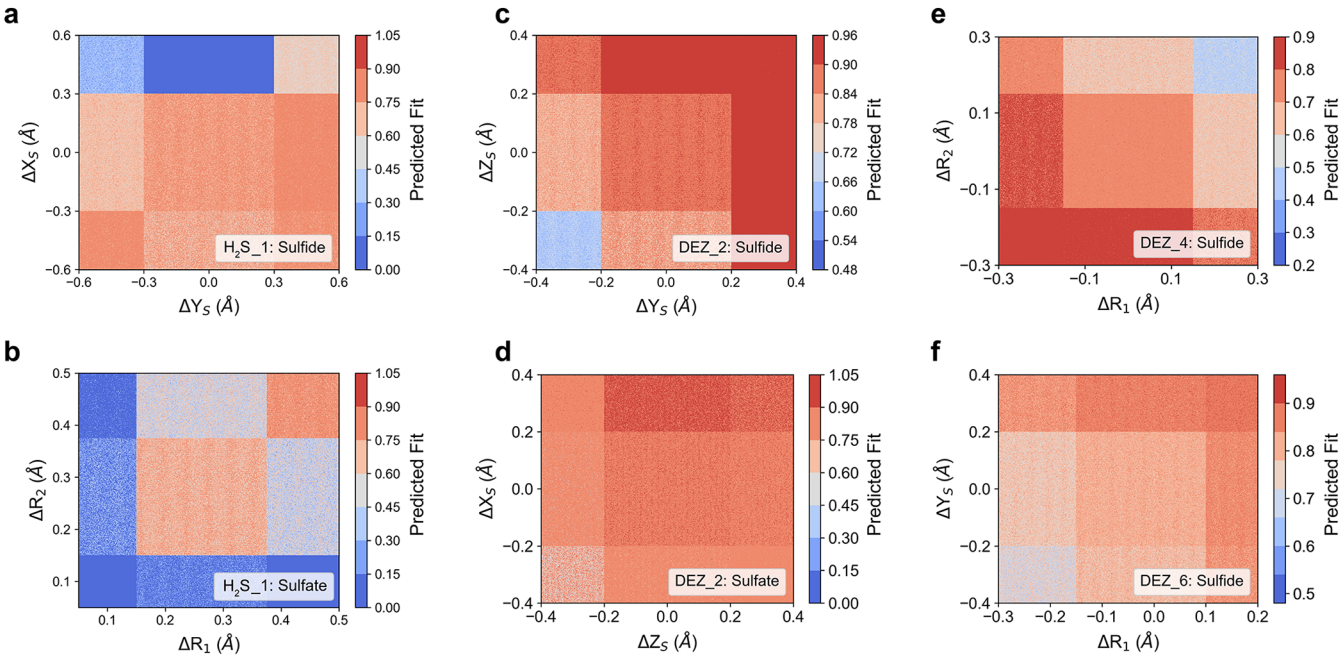

Figure 6. Response surfaces plotted of the most important parameters on each trained RF model for H_2S_1, sulfide (a); H_2S_1, sulfate (b); DEZ_2, sulfide (c); DEZ_2, sulfate (d); DEZ_4, sulfide (e); and DEZ_6, sulfide (f). In regions where the response surfaces appear more "speckled", the remaining parameters have a relatively more significant impact on the predicted Fit. Conversely, uniformly colored regions that appear "solid" in the response surfaces indicate that the values of the two most important parameters are sufficient to predict the Fit value.

After the third DEZ pulse (DEZ_6), we expect the surface reactions to be similar to the second DEZ pulse (DEZ_4). The initial atomic model is built by using results from the previous data set (DEZ_4) and incorporating 4-fold coordinated sulfur atoms. Because there were multiple viable atomic arrangements from DEZ_4, inputs to DEZ_6 were manually inspected and selected from arrangements that had a Fit value greater than 0.9.

As shown in Figure 5e, the profile of the S−K edge trends downward in the range between 2475 and 2480 eV. Thus, we expect the coordination environment of the S atoms to be quantitatively different between the DEZ_4 and DEZ_6 atomic structure models that yield the best Fit. As in DEZ_4, ΔR_1 and ΔR_2 are important structural parameters, but in DEZ_6 they have combined importance of less than 50%. In DEZ_6, ΔY_S is also an important structural parameter. In the Discussion section, the influence of the most important structural parameters on the Fit will be used to provide insight into the evolution of the coordination environment of the S atoms.

DISCUSSION

From the in situ S K-edge spectra, we were able to deduce three oxidation states present in the initial half-cycles. The evolving S−K edge spectra after each cycle contain information on the mechanism of how the approximated initial sulfide and sulfate species on the TiO_2 surface transform into a crystalline ZnS film. By simulating the XANES spectra of hundreds of atomic arrangements in the initial half cycles and applying ML models to analyze the resulting data sets, we were able to identify atomic arrangements that provide insight into structural rearrangements during film growth. As a result, we now have a trained ML model that can be used to explore a larger space of atomic configurations and predict the Fit without having to run new FEFF9 simulations.

Central to this discussion is the collection of response surfaces for the data sets using the trained RF models (Figure 6). These response surfaces help visualize how a system responds to a set of parameters. In this case, the focus is understanding how the predicted Fits between the experimental and simulated XANES spectra respond to changes in the structural parameters. The initial ranges of the two most important structural parameters are used to create a two-dimensional grid of values that will serve as the foundation for the response surface. To generate a set of input values for the remaining structural parameters, we used a uniform distribution of each parameter within a specified range (further details in the SI). Using a uniform distribution creates speckled regions in the response surfaces, which indicate how sensitive the predicted Fit is to changes in the remaining parameters. For regions in the response surface that appear more "speckled", meaning they have a more extensive color gradient between pixels, the remaining parameters have a relatively more significant impact on the predicted Fit. Conversely, uniformly colored regions that appear "solid" in the response surfaces indicate that the values of the two most important parameters are sufficient to predict the Fit value. This approach is the basis for all the response surfaces in Figure 6.

In Figure 6a, the response surface for the sulfide region in H_2S_1 depicts an overall trend of predicted Fit values greater than 0.6 when changes in the S X position are below 0.3 Å. Moving the Y position of the S atom, a distance between 0.3 and 0.6 Å in either the positive or the negative direction resulted in predicted Fit values greater than 0.75. This mirrored response is consistent with the fact that the local coordination environment of the S atom is nearly symmetric about the X-axis, as shown in Figure 3a. The response surface shows that there is a clear preference for the S atom in Figure 3a to move off the XZ plane created by the bonded Ti surface atoms.

DOI: 10.1021/acs.chemmater.9b03025
Chem. Mater. 2019, 31, 8937−8947

For the H_2S_1 sulfate response surface (Figure 6b), there is a clear trend that atomic arrangements are predicted to have larger Fit values when increasing the bond lengths between the S and O ligands (ΔR_1 and ΔR_2) concurrently by more than 0.15 Å. Given the sulfate species created as described in eq 2, these models suggest that the ligand O atoms on the S are in equivalent chemical states.

After the first DEZ pulse, the DEZ molecules have reacted with the surface sulfide and sulfate species. From the sulfide response surface in Figure 6c, there is a pronounced trend toward larger predicted Fit values with increasing the Y and Z coordinates of the S atom. This trend indicates that the ligand exchange between the S atom and MEZ species causes the S atom to elongate from the Ti atoms in both the Y and the Z directions. There is an overall expansion of the S−Ti bonds when the MEZ species is present. The increase in Ti−S bond lengths is an expected consequence of the S atom and the Zn forming a Lewis acid−base pair. In contrast with the DEZ_2 sulfide response surface, there is no well-defined trend in the DEZ_2 sulfate response surface (Figure 6d). A possible explanation for this difference is that a bonding MEZ ligand to the sulfate species, as shown in Figure 3d, causes small readjustments of the atomic position of the S atom.

As mentioned earlier, after the second DEZ pulse (DEZ_4), the resulting MEZ species are likely starting to form a tetrahedral coordination environment around the S atoms, as indicated by the transition in the shape of the S K-edge profile. As shown in the DEZ_4 sulfide response surface in Figure 6e, there is a clear trend of larger predicted Fit values when the S−Zn bond lengths (ΔR_1 and ΔR_2) decrease. A possible explanation for the S−Zn bond length contraction is that the second DEZ pulse causes surface reconstructions that start to resemble more of a symmetric 4-fold coordination.

In the DEZ_6 sulfide response surface (Figure 6f), there is a clear trend with larger predicted Fit values with increasing ΔY_s and ΔR_1. These increases indicate that the coordination environment around the S atom expands again after the third DEZ pulse. A possible explanation for this expansion following the preceding contraction in the S−Zn bond lengths indicates that there are enough Zn−S species on the TiO_2 surface at this point to start forming a discernible ZnS film. This discernible ZnS film is a reasonable explanation since the ZnS region of the S−K edge spectra for subsequent cycles beyond DEZ_6 does not change in its overall shape (Figure 2).

CONCLUSION

In this work, we have developed insight into the dynamic evolution of atomic structure during ALD reactions by using in situ XANES studies and harnessing machine learning strategies. Through experimental measurements and a simulation framework, the detailed atomic structure evolution of a growing ZnS film on a nanostructured TiO_2 substrate was described. Experimentally, the formation of sulfide and sulfate species was observed after the first H_2S pulse. Subsequent ALD cycles resulted in the continuous development of the coordination and oxidation environment of ZnS, as captured by the convergence of the S K-edge spectra of the growing film with that of the ZnS references. The likely atomic arrangements that describe the structural evolution during the initial ALD cycles were identified through high-throughput screening of atomic arrangements, based on the similarity between their simulated S K-edge spectra with the corresponding in situ spectra. As a result of the screening, it is evident that (a) the initial sulfate species are buried at the interface between the TiO_2 and growing ZnS; (b) by the fourth ALD half cycle, the sulfur species are in a 4-fold coordination environment; and (c) by the sixth half cycle, the sulfur species are in a coordination environment that closely resembles the crystalline ZnS structure. This work provides an example of a framework that can be adapted and leveraged when carrying high-throughput experimental measurements coupled with high-throughput calculations. In future work, it will be possible to use this approach to gain a richer understanding of surface reactions, interfacial structure development, and thin-film growth.

ASSOCIATED CONTENT

Supporting Information

The Supporting Information is available free of charge on the ACS Publications website at DOI: 10.1021/acs.chemmater.9b03025.

Methods of material preparation, modeling, supplementary characterizations, and additional discussion and figures (PDF)

AUTHOR INFORMATION

Corresponding Author

*(N.P.D.) E-mail: ndasgupt@umich.edu.

ORCID

Ritimukta Sarangi: 0000-0002-2764-2279
Jan Torgersen: 0000-0003-1675-8759
Neil P. Dasgupta: 0000-0002-5180-4063

Author Contributions

¶(O.T. and A.L.D.) These authors contributed equally to this work

Notes

The authors declare no competing financial interest.

ACKNOWLEDGMENTS

O.T. acknowledges the support of a Department of Energy (DOE) EERE Postdoctoral Research Award and Stanford University's Diversifying Academia, Recruiting Excellence (DARE) Fellowship. This material is based upon work supported by the National Science Foundation under Grant No. 1727918. A.L.D. was funded by the Norwegian Research Council under Project Number 274459 Trånslate. J.T. acknowledges funds from the Austrian Research Fund (FWF) under Contract NJ3505-N20. The authors further thank the Stanford Nano Shared Facilities (SNSF), for use of PHI VersaProbe Scanning XPS Microprobe for XPS measurements. We thank K. Roelofs and S. Bent for materials and consultations. We also thank SLAC for allowing us to gather data using beamlines 4-3 at SSRL.

REFERENCES

(1) Sofia, S. E.; Mailoa, J. P.; Weiss, D. N.; Stanbery, B. J.; Buonassisi, T.; Peters, I. M. Economic Viability of Thin-Film Tandem Solar Modules in the United States. *Nat. Energy* **2018**, *3* (5), 387−394.

(2) Yu, Z. J.; Carpenter, J. V.; Holman, Z. C. Techno-Economic Viability of Silicon-Based Tandem Photovoltaic Modules in the United States. *Nat. Energy* **2018**, *3* (9), 747−753.

(3) Myny, K. The Development of Flexible Integrated Circuits Based on Thin-Film Transistors. *Nat. Electron.* **2018**, *1* (1), 30−39.

DOI: 10.1021/acs.chemmater.9b03025
Chem. Mater. 2019, 31, 8937−8947

(4) Gambetta, J. M.; Chow, J. M.; Steffen, M. Building Logical Qubits in a Superconducting Quantum Computing System. *npj Quantum Inf* **2017**, *3* (1), 2.
(5) George, S. M. Atomic Layer Deposition: An Overview. *Chem. Rev.* **2010**, *110* (1), 111−131.
(6) Elliott, S. D.; Dey, G.; Maimaiti, Y.; Ablat, H.; Filatova, E. A.; Fomengia, G. N. Modeling Mechanism and Growth Reactions for New Nanofabrication Processes by Atomic Layer Deposition. *Adv. Mater.* **2016**, *28* (27), 5367−5380.
(7) Knapas, K.; Ritala, M. *In Situ* Studies on Reaction Mechanisms in Atomic Layer Deposition. *Crit. Rev. Solid State Mater. Sci.* **2013**, *38* (3), 167−202.
(8) Trejo, O.; Roelofs, K. E.; Xu, S.; Logar, M.; Sarangi, R.; Nordlund, D.; Dadlani, A. L.; Kravec, R.; Dasgupta, N. P.; Bent, S. F.; et al. Quantifying Geometric Strain at the PbS QD-TiO2 Anode Interface and Its Effect on Electronic Structures. *Nano Lett.* **2015**, *15* (12), 7829−7836.
(9) Dadlani, A. L.; Trejo, O.; Acharya, S.; Torgersen, J.; Petousis, I.; Nordlund, D.; Sarangi, R.; Schindler, P.; Prinz, F. B. Exploring the Local Electronic Structure and Geometric Arrangement of ALD Zn(O,S) Buffer Layers Using X-Ray Absorption Spectroscopy. *J. Mater. Chem. C* **2015**, *3* (47), 12192−12198.
(10) Dadlani, A. L.; Acharya, S.; Trejo, O.; Prinz, F. B.; Torgersen, J. ALD Zn(O,S) Thin Films' Interfacial Chemical and Structural Configuration Probed by XAS. *ACS Appl. Mater. Interfaces* **2016**, *8* (23), 14323−14327.
(11) Jalilehvand, F. Sulfur: Not a "Silent" Element Any More. *Chem. Soc. Rev.* **2006**, *35* (12), 1256−1268.
(12) Rehr, J. J.; Albers, R. C. Theoretical Approaches to X-Ray Absorption Fine Structure. *Rev. Mod. Phys.* **2000**, *72* (3), 621−654.
(13) Rehr, J. J.; Kas, J. J.; Prange, M. P.; Sorini, A. P.; Takimoto, Y.; Vila, F. Ab Initio Theory and Calculations of X-Ray Spectra. *C. R. Phys.* **2009**, *10* (6), 548−559.
(14) Rehr, J. J.; Kas, J. J.; Vila, F. D.; Prange, M. P.; Jorissen, K. Parameter-Free Calculations of X-Ray Spectra with FEFF9. *Phys. Chem. Chem. Phys.* **2010**, *12*, 5503−5513.
(15) Mathew, K.; Zheng, C.; Winston, D.; Chen, C.; Dozier, A.; Rehr, J. J.; Ong, S. P.; Persson, K. A. High-Throughput Computational X-Ray Absorption Spectroscopy. *Sci. Data* **2018**, *5*, 180151.
(16) Devloo-Casier, K.; Ludwig, K. F.; Detavernier, C.; Dendooven, J. In Situ Synchrotron Based X-Ray Techniques as Monitoring Tools for Atomic Layer Deposition. *J. Vac. Sci. Technol., A* **2014**, *32* (1), 010801.
(17) Baldo, P. M.; Highland, M. J.; Fong, D. D.; Fuoss, P. H.; Kim, S. K.; Eastman, J. A.; Fister, T. T. In Situ Synchrotron X-Ray Characterization of ZnO Atomic Layer Deposition. *Appl. Phys. Lett.* **2010**, *97* (19), 191904.
(18) Boichot, R.; Tian, L.; Richard, M. I.; Crisci, A.; Chaker, A.; Cantelli, V.; Coindeau, S.; Lay, S.; Ouled, T.; Guichet, C.; et al. Evolution of Crystal Structure during the Initial Stages of ZnO Atomic Layer Deposition. *Chem. Mater.* **2016**, *28* (2), 592−600.
(19) Mack, J. F.; Van Stockum, P. B.; Yemane, Y. T.; Logar, M.; Iwadate, H.; Prinz, F. B. Observing the Nucleation Phase of Atomic Layer Deposition in Situ. *Chem. Mater.* **2012**, *24* (22), 4357−4362.
(20) Billinge, S. J. L.; Levin, I. The Problem with Determining Atomic Structure at the Nanoscale. *Science (Washington, DC, U. S.)* **2007**, *316* (5824), 561−565.
(21) Timoshenko, J.; Lu, D.; Lin, Y.; Frenkel, A. I. Supervised Machine-Learning-Based Determination of Three-Dimensional Structure of Metallic Nanoparticles. *J. Phys. Chem. Lett.* **2017**, *8* (20), 5091−5098.
(22) Zheng, C.; Mathew, K.; Chen, C.; Chen, Y.; Tang, H.; Dozier, A.; Kas, J. J.; Vila, F. D.; Rehr, J. J.; Piper, L. F. J. Automated Generation and Ensemble-Learned Matching of X-Ray Absorption Spectra. *npj Comput. Mater.* **2018**, *4* (1), 12.
(23) Carbone, M. R.; Yoo, S.; Topsakal, M.; Lu, D. Classification of Local Chemical Environments from X-Ray Absorption Spectra Using Supervised Machine Learning. *Phys. Rev. Mater.* **2019**, *3* (3), 033604.
(24) Ke, W.; Stoumpos, C. C.; Logsdon, J. L.; Wasielewski, M. R.; Yan, Y.; Fang, G.; Kanatzidis, M. G. TiO2-ZnS Cascade Electron Transport Layer for Efficient Formamidinium Tin Iodide Perovskite Solar Cells. *J. Am. Chem. Soc.* **2016**, *138* (45), 14998−15003.
(25) Kokal, R. K.; Deepa, M.; Kalluri, A.; Singh, S.; Macwan, I.; Patra, P. K.; Gilarde, J. Solar Cells with PbS Quantum Dot Sensitized TiO2-Multiwalled Carbon Nanotube Composites, Sulfide-Titania Gel and Tin Sulfide Coated C-Fabric. *Phys. Chem. Chem. Phys.* **2017**, *19* (38), 26330−26345.
(26) Shaikh, S. F.; Kwon, H. C.; Yang, W.; Mane, R. S.; Moon, J. Performance Enhancement of Mesoporous TiO2 -Based Perovskite Solar Cells by ZnS Ultrathin-Interfacial Modification Layer. *J. Alloys Compd.* **2018**, *738*, 405−414.
(27) Bakke, J. R.; King, J. S.; Jung, H. J.; Sinclair, R.; Bent, S. F. Atomic Layer Deposition of ZnS via in Situ Production of H2S. *Thin Solid Films* **2010**, *518* (19), 5400−5408.
(28) Mack, J. F.; Van Stockum, P. B.; Yemane, Y. T.; Logar, M.; Iwadate, H.; Prinz, F. B. Observing the Nucleation Phase of Atomic Layer Deposition in Situ. *Chem. Mater.* **2012**, *24* (22), 4357−4362.
(29) Dasgupta, N. P.; MacK, J. F.; Langston, M. C.; Bousetta, A.; Prinz, F. B. Design of an Atomic Layer Deposition Reactor for Hydrogen Sulfide Compatibility. *Rev. Sci. Instrum.* **2010**, *81* (4), 044102.
(30) Ong, S. P.; Richards, W. D.; Jain, A.; Hautier, G.; Kocher, M.; Cholia, S.; Gunter, D.; Chevrier, V. L.; Persson, K. A.; Ceder, G. Python Materials Genomics (Pymatgen): A Robust, Open-Source Python Library for Materials Analysis. *Comput. Mater. Sci.* **2013**, *68*, 314−319.
(31) Pedregosa, F.; Michel, V.; Grisel, O.; Blondel, M.; Prettenhofer, P.; Weiss, R.; Vanderplas, J.; Cournapeau, D.; Varoquaux, G.; Gramfort, A. et al. *Scikit-Learn: Machine Learning in Python*; Packt Publishing Ltd.: Birmingham, 2011; Vol. *12*.
(32) Momma, K.; Izumi, F. VESTA 3 for Three-Dimensional Visualization of Crystal, Volumetric and Morphology Data. *J. Appl. Crystallogr.* **2011**, *44* (6), 1272−1276.
(33) *JMP*, version 14; SAS Institute Inc.: Cary, NC, 2019.
(34) Butler, K. T.; Davies, D. W.; Cartwright, H.; Isayev, O.; Walsh, A. Machine Learning for Molecular and Materials Science. *Nature* **2018**, *559* (7715), 547−555.
(35) Breiman, L. Random Forests. *Mach. Learn.* **2001**, *45* (1), 5−32.
(36) Strobl, C.; Boulesteix, A. L.; Zeileis, A.; Hothorn, T. Bias in Random Forest Variable Importance Measures: Illustrations, Sources and a Solution. *BMC Bioinf.* **2007**, *8*, 25.
(37) Law, A. M.; Kelton, W. D. *Simulation Modeling and Analysis*, 3rd ed.; McGraw-Hill Higher Education: New York, 2000.
(38) Fleet, M. E.; Harmer, S. L.; Liu, X.; Nesbitt, H. W. Polarized X-Ray Absorption Spectroscopy and XPS of TiS3: S K- and Ti L-Edge XANES and S and Ti 2p XPS. *Surf. Sci.* **2005**, *584* (2−3), 133−145.
(39) Dathe, H.; Jentys, A.; Lercher, J. A. In Situ S K-Edge X-Ray Absorption Spectroscopy for Understanding and Developing so x Storage Catalysts. *J. Phys. Chem. B* **2005**, *109* (46), 21842−21846.
(40) Rodriguez, J. A.; Chaturvedi, S.; Kuhn, M.; Hrbek, J. Reaction of H2S and S2 with Metal/Oxide Surfaces: Band-Gap Size and Chemical Reactivity. *J. Phys. Chem. B* **1998**, *102* (28), 5511−5519.
(41) Yanxin, C.; Yi, J.; Wenzhao, L.; Rongchao, J.; Shaozhen, T.; Wenbin, H. Adsorption and Interaction of H2S/SO2 on TiO2. *Catal. Today* **1999**, *50* (1), 39−47.
(42) Huang, W. F.; Chen, H. T.; Lin, M. C. Density Functional Theory Study of the Adsorption and Reaction of H2S on TiO2 Rutile (110) and Anatase (101) Surfaces. *J. Phys. Chem. C* **2009**, *113* (47), 20411−20420.
(43) Duan, Y.; Pirolli, L.; Teplyakov, A. V. Investigation of the H2S Poisoning Process for Sensing Composite Material Based on Carbon Nanotubes and Metal Oxides. *Sens. Actuators, B* **2016**, *235*, 213−221.
(44) Junkaew, A.; Maitarad, P.; Arróyave, R.; Kungwan, N.; Zhang, D.; Shi, L.; Namuangruk, S. The Complete Reaction Mechanism of H2S Desulfurization on an Anatase TiO2 (001) Surface: A Density Functional Theory Investigation. *Catal. Sci. Technol.* **2017**, *7* (2), 356−365.

DOI: 10.1021/acs.chemmater.9b03025
Chem. Mater. 2019, 31, 8937−8947

(45) Gong, X.-Q.; Selloni, A.; Batzill, M.; Diebold, U. Steps on Anatase TiO2(101). *Nat. Mater.* **2006**, *5* (8), 665−670.
(46) Weckman, T.; Laasonen, K. Atomic Layer Deposition of Zinc Oxide: Diethyl Zinc Reactions and Surface Saturation from First-Principles. *J. Phys. Chem. C* **2016**, *120* (38), 21460−21471.

DOI: 10.1021/acs.chemmater.9b03025
Chem. Mater. 2019, 31, 8937−8947